Journal of Materials Chemistry A

Zinc(II) Complex of Di(naphthylethynyl)azadipyrromethene with low synthetic complexity leads to OPV with high industrial accessibility

Journal:	*Journal of Materials Chemistry A*
Manuscript ID	TA-ART-08-2019-008654.R1
Article Type:	Paper
Date Submitted by the Author:	19-Sep-2019
Complete List of Authors:	Wang, Chunlai; Case Western Reserve University, Chemistry Wei, Peiran; Case Western Reserve University, Chemistry Ngai, Jenner Ho Loong; University of Waterloo, Chemical Engineering Rheingold, Arnold; University of California San Diego, Department of Chemistry and Biochemistry Gray, Thomas; Case Western Reserve University, Chemistry Li, Yuning; University of Waterloo, Chemical Engineering and Waterloo Institute for Nanotechnology Pentzer, Emily; Texas A&M University System, Chemistry, Materials Science and Engineering Li, Ruipeng; National Synchrotron Light Source Zhu, Lei; Case Western Reserve University, Macromolecular Science and Engineering Sauve, Genevieve; Case Western Reserve University, Chemistry

ARTICLE

Zinc(II) Complex of Di(naphthylethynyl)azadipyrromethene with low synthetic complexity leads to OPV with high industrial accessibility

Received 00th January 20xx,
Accepted 00th January 20xx

DOI: 10.1039/x0xx00000x

Chunlai Wang,[a] Peiran Wei,[a] Jenner H.L. Ngai,[b] Arnold L. Rheingold,[c] Thomas G. Gray,[a] Yuning Li,[b] Emily Pentzer,[a] Ruipeng Li,[d] Lei Zhu,[e] and Genevieve Sauvé [a, †]

Organic photovoltaics have reached high power conversion efficiencies (PCE) using non-fullerene acceptors (NFA). However, the best NFAs tend to have complex syntheses, limiting scalability. Among polymer donors, regioregular poly(3-hexylthiophene) (P3HT) has the greatest potential for commercialization due to its simple synthesis and good stability, but PCEs have been limited. It is thus imperative to find scalable NFAs that give high PCE with P3HT. We report a zinc(II) complex of di(naphthylethynyl)azadipyrromethene ($Zn(L2)_2$) as a non-planar NFA that can be synthesized on the gram scale using inexpensive starting materials without chromatography column purification. The NFA has strong absorption in the 600–800 nm region. Time-dependent density-functional theory calculations suggest that the low-energy absorptions can be understood within a four-orbital model involving transitions between π-orbitals on the azadipyrromethene core. OPVs fabricated from P3HT:$Zn(L2)_2$ blends reached a PCE of 5.5%, and the PCE was not very sensitive to the P3HT:$Zn(L2)_2$ weight ratio. Due to its shape, $Zn(L2)_2$ shows isotropic charge transport and its potential as an electron donor is also demonstrated. The combination of simple synthesis, good PCE and photostability, and tolerance to active material weight ratio demonstrates the potential for $Zn(L2)_2$ as an active layer material in OPVs.

Introduction

Solution processed organic photovoltaics (OPVs) are promising devices for the conversion of solar energy into electricity due to their attractive properties of low-cost, light weight, flexibility, aesthetic appearance (colored or semitransparent) and non-toxicity.[1-3] The active layer of OPVs typically consists of a blend of two conjugated compounds: an electron donor and an electron acceptor. Until recently, fullerene-derivatives were favored as electron acceptor, but it became clear that using fullerene-derivatives as acceptor severely limits device performance, stability and mechanical flexibility. This drove research in the synthesis and application of non-fullerene acceptors (NFAs). Research over the last decade has demonstrated that NFAs are promising for overcoming many of these limitations, with PCEs for single junction OPV reaching 16%,[4-11] and reports of better mechanical properties and stability.[12-16] However, most of the research on active materials has aimed at improving PCE, often without considering other important factors required for commercialization, such as cost and synthetic scalability.[17] As a result, most high-performance donor and acceptor materials contain pricy building blocks or have high synthetic complexity.[18-20] This is an important issue considering that the overall cost of an OPVs technology heavily depends on the material cost.[20]

Estimating the industrial cost and scalability of active layer materials is difficult. Pellegrino and co-workers proposed a more convenient but indirect way to estimate cost by calculating the synthetic complexity (SC), assessed from five parameters: number of synthetic steps (NSS), reciprocal yield (RY), number of operation units for isolation or purification (NUO), number of chromatography columns (NCC) and number of hazardous chemicals (NHC).[18] Each parameter is related to the maximum number obtained from a list of 92 high performance conjugated polymer donors analyzed, and weighted for its importance using the following equation:

$$SC = 35\frac{NSS}{NSS_{max}} + 25\frac{logRY}{logRY_{max}} + 15\frac{NUO}{NUO_{max}} + 15\frac{NCC}{NCC_{max}} + 10\frac{NHC}{NHC_{max}}$$

Equation (1)

The obtained SC is therefore a percentage relative to a maximum number, and the lower the percentage, the better. Regioregular poly(3-hexylthiophene) (P3HT) had by far the lowest SC of the 92 polymer donors analyzed, at 7.7%. For comparison, the higher performance polymer polythieno[3,4-

---

[a] Department of Chemistry, Case Western Reserve University, Cleveland, Ohio 44106-7078, United States.
[b] Department of Chemical Engineering and Waterloo Institute for Nanotechnology (WIN) University of Waterloo, Waterloo, Ontario, Canada, N2L 3G1.
[c] Department of Chemistry and Biochemistry, University of California, San Diego, La Jolla, California 92093, United States.
[d] National Synchrotron Light Source II, Brookhaven National Laboratory, Upon, New York 11973, United States.
[e] Department of Macromolecular Science and Engineering, Case Western Reserve University, Cleveland, Ohio 44106-7202, United States.
† Corresponding author, E-mail: genevieve.sauve@case.edu (G.S.).

Electronic Supplementary Information (ESI) available: [details of any supplementary information available should be included here]. See DOI: 10.1039/x0xx00000x b]-thiophene-co-benzodithiophene (PTB7) has a SC of 58%. For electron acceptors, only a few SC indexes are reported, and also tend to be high. For example, phenyl-C_{61}-butyric acid methyl ester (PCBM) is the lowest at ~20%. The high performance NFA 3,9-bis(2-methylene-(3-(1,1-dicyanomethylene)-indanone))-5,5,11,11-tetrakis(4-hexylphenyl)-dithieno[2,3-d:2′,3′-d′]-s-indaceno[1,2-b:5,6-b′]dithiophene (ITIC) has a SC of ~57%.[20-21] Low SC materials tend to have simple structure and straightforward synthesis, such as P3HT. It is not surprising that P3HT is currently the only high-efficiency polymer donor that is available on a large scale (>10 kg).[17]

Recently, a high performance solar cell was reported to use low cost materials: (poly{(thiophene)-alt-[6,7-difluoro-2-(2 hexyldecyloxy)quinoxaline]} (PTQ10) as the donor and (6-fluoro-[3-(1,1-dicyanomethylene)-indanone]-4,4,9,9-tetrahexyl-5,10-dimethoxyl-4,9-dihydro-s-indaceno [1,2-b:5,6-b′] dithiophene} (MO-IDIC-2F)) as the acceptor.[5, 22] Their cost calculation is based on cost of chemicals and solvents, but does not take into account labor costs. For better comparison, we calculated a SC of the two materials using the reported experimental details and obtained 14.8% for PTQ10 and 25.2% for MO-IDIC-2F (see Table S10 and S11).

To better evaluate the potential of an active layer blend for commercialization, it is also important to consider solar cell performance and stability.[18, 20, 23] A new index, called the industrial figure of merit (i-FoM) considers these factors and can be calculate using the equation:

$$i - FoM = \frac{PCE \times Photostability}{SC} \qquad \text{Equation (2)}$$

where the photostability data is from a normal device under illumination and inert atmosphere for 200 h.[20] Using this equation, the higher the number, the better the overall performance. In the best case scenario, Li, Brabec and co-workers estimate that if a blend had as low a SC as P3HT:PCBM but also photostability of 1.0 and maximum theoretical efficiency of 19.8%, a high i-FoM of 1.3 would be obtained.[23] The authors proposed a benchmark i-FoM of 0.7 using a PCE of 10% and a photostability of 0.98. The i-FoM for the blend with the lowest SC, P3HT:PCBM, is only 0.18 due to the low PCE of 2.8%. On the other hand, by replacing P3HT with the high performance poly[(5,6-difluoro-2,1,3-benzothiadiazol-4,7-diyl)-*alt*-(3,3′′′-di(2-octyldodecyl)-2,2′;5′,2′′;5′′,2′′′-quaterthiophen-5,5′′′-diyl)] (PCE11), PCE increased to 9.2%, but the i-FoM only increased to 0.26 due to the high SC of the PCE11:PCBM blend. The i-FoM of the recently reported PTQ10:Mo-IDIC-2F blend has not been reported and cannot be calculated because the photostability is not reported. However, if we assumed a photostability of 0.8, an i-FoM of 0.5 would be obtained, illustrating the importance of lowering SC while maximizing PCE to increase i-FoM.

We note that to obtain the highest theoretical PCE of 19.8%, Li, Brabec and co-workers found that the hypothetical NFA should have a bandgap of 1.4 eV while the polymer donor bandgap can range from 1.6 to 1.9 eV, i.e., it was not sensitive to the polymer donor's bandgap. In this case, the preferred polymer donor for commercialization would therefore be one with good photostability and low SC, such as P3HT. To our knowledge, the highest PCE for a P3HT based OPV is 6.4%,[13] but the i-FoM is only 0.23 due to the high SC of the NFA. We therefore favor developing novel NFAs that have low SC and that give high PCE and photostability when blended with P3HT.

In the past, we reported a promising class of NFAs based on homoleptic zinc(II) complexes of di(phenylethynyl)azadipyrromethene, $Zn(WS3)_2$ in Figure 1.[24-25] This complex has high electron affinity and high absorption between 600 and 800 nm, complementary to P3HT. The non-planarity of the complex contributes to favorable nanoscale phase separation from P3HT. Moreover, these complexes are relatively easy to synthesize from cheap and readily accessible starting materials. However, P3HT:$Zn(WS3)_2$ typically have PCE of around 2.5%, too low for practical applications.[26-27] Substituting the pyrrolic phenylethynyl groups with thiophene, thienylethynyl or styryl groups have not improved performance.[28-29] On the other hand, fluorination at the *para* position of the phenylethynyls improved PCE to 3.7% and significantly increased electron mobility.[26] The only crystal structure of a $Zn(WS3)_2$ derivative we had prior to this report was for the complex with F at the *para* distal phenyls, and it showed intermolecular interactions between the pyrrolic phenyls of two neighboring molecules.[30] Based on these results, we hypothesized that the aromatic group on the pyrrolic substituent plays an important role in charge transport.

To test this hypothesis, we replaced the phenyl in the pyrrolic phenylethynyl groups with a larger aromatic group in order to enhance intermolecular π-π interactions and charge transport. Naphthalene was chosen because the starting material is inexpensive and readily available. After a few synthetic experiments, it became apparent that replacing the phenyl units with naphthyl groups significantly reduced solubility in organic solvent. It was therefore necessary to add solubilizing groups. Herein, we report the synthesis and properties of two new complexes: $Zn(L1)_2$, and $Zn(L2)_2$ (see Figure 1). $Zn(L1)_2$ is derived from $Zn(WS3)_2$ with hexyl groups at the *para* position of the proximal phenyls. $Zn(L2)_2$ is derived from $Zn(L1)_2$ with 1-naphthylethynyl groups at the pyrrolic positions. The complexes were fully characterized and tested in OPVs using P3HT as the donor. $Zn(L2)_2$ exhibits interesting properties such as ambipolarity and isotropic charge transport. Moreover, the SC of $Zn(L2)_2$ was calculated to be 22.1%, which is lower than most existing high performance NFAs, and when combined with an OPV PCE of 5.5% and 200 h photostability of 81%, a high i-FoM of 0.30 was achieved, getting closer to the benchmark of 0.7 thought to be required for commercialization.

Result and Discussion

Synthesis

Scheme 1 summarizes the synthesis of $Zn(L1)_2$ and $Zn(L2)_2$. First, the ADP ligand with proximal (abbreviated as *pr*) hexyl solubilizing groups (*pr*-hexylADP) was synthesized from the appropriate hexyl-functionalized starting materials.[31] In order

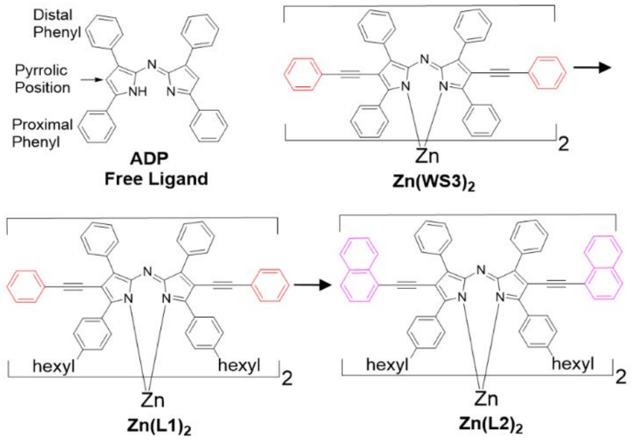

Figure 1. Chemical Structure of ADP and zinc(II) complexes.

to install pyrrolic substituents, the ligand was then iodinated to obtain a dark blue product, *pr*-hexylADPI$_2$.[28, 30] Pyrrolic substituents were installed by reacting the appropriate tributyl tin compounds with *pr*-hexylADPI$_2$ using Stille coupling conditions. [28] The reaction was monitored using MALDI-TOF MS and found to be complete in about 6 h, much less time than the 48 h required for completion of the synthesis of the iodinated ligands without hexyl groups.[28, 30] This faster reaction time is thought to be due to the improved solubility of the free ligands with hexyl groups. The ligands L1 and L2 were purified by washing with methanol and were isolated as dark blue powders in very good yields (~90%). L1 and L2 were slightly soluble in non-polar solvent, such as hexanes, and readily soluble in polar solvents, such as acetone and dichloromethane.

The zinc(II) complexes were synthesized using our published procedure in good yields.[30] Both Zn(L1)$_2$ and Zn(L2)$_2$ were easier to purify than Zn(WS3)$_,$ which contains no hexyl groups. Zn(L1)$_2$ still required column chromatography to obtain a pure product, but a shorter column (~8 inch) was required than for other Zn(WS3)$_2$ derivatives (~15 inch) due to the higher solubility and lower polarity of Zn(L1)$_2$. The product Zn(L1)$_2$ was collected

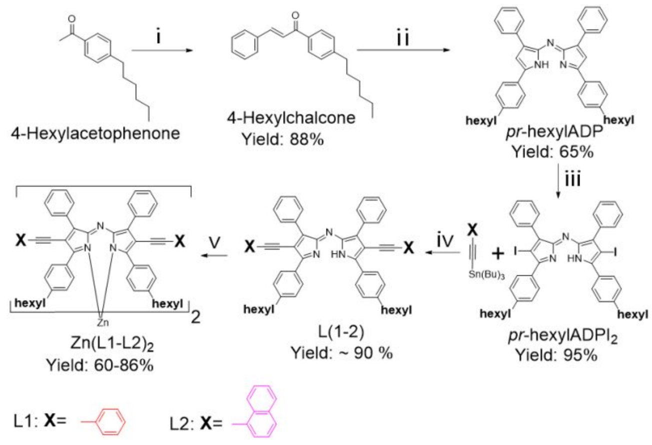

Scheme 1. Synthesis scheme for zinc(II) complexes: Zn(L1)$_2$ and Zn(L2)$_2$. (i) MeOH, 5M NaOH, 25°C, 24 h (ii) MeNO$_2$, DEA, MeOH, reflux, 24 h; ammonium acetate, 1-butanol, reflux, 24 h, (iii) NIS, CHCl$_3$, acetic acid, 25°C, 12 h under dark, (iv) Pd(PPh$_3$)$_4$, xylenes, 125°C, 8 h, (v) THF, NaH, 55°C, 4h, followed by CH$_2$Cl$_2$, ZnCl$_2$/MeOH, 25°C, 24 h.

from the first blue colored fraction, and the yield of Zn(L1)$_2$, 61%, was higher than the yield of Zn(WS3)$_2$, 54%.[28] In contrast, Zn(L2)$_2$ did not require any column to obtain a pure compound. Instead, pure Zn(L2)$_2$ was obtained by washing the product with methanol to remove salt and polar impurities, and acetone to remove unreacted ligand. The Zn(L2)$_2$ was then extracted with dichloromethane to give a dark blue solid in 86% yield. The high yield of Zn(L2)$_2$ was attributed to the easy purification method. The identity and purity of the complexes were confirmed by ^{1}H NMR, MADI-TOF MS and elemental analysis (see Supporting Information). The combination of easy synthesis from readily accessible building blocks with no column chromatography required enables easier scale up of Zn(L2)$_2$ than most existing non-fullerene acceptors.

Optical and Electrochemical Properties

The UV-Vis absorption spectra of Zn(L1-L2)$_2$ in chloroform are shown in Figure 2 and summarized in Table 1. The spectrum of Zn(WS3)$_2$ is included for comparison. The spectrum of Zn(L1)$_2$ is

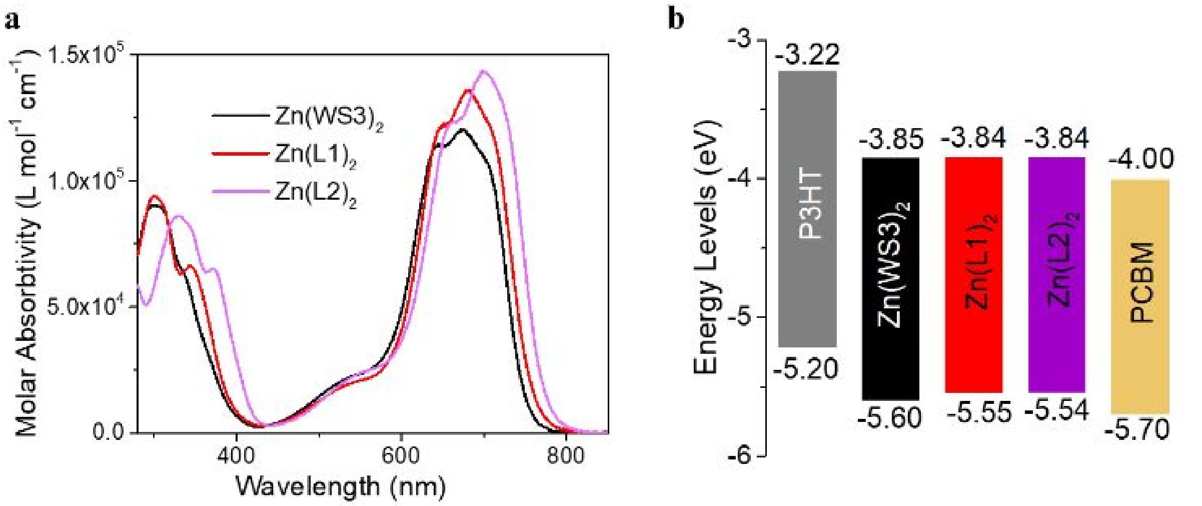

Figure 2. a) UV-Vis absorption spectra of zinc(II) complexes in chloroform. b) Estimated HOMO and LUMO energy levels obtained by cyclic voltammetry. The energy levels for P3HT were estimated using the oxidation onset in films and optical gap.[45] The energy levels of all molecular electron acceptors were obtained under the same conditions in our laboratory, from the E1/2 values in dichloromethane and using the value of −5.1 eV for Fc/Fc+.[24]

Table 1. Summary of optical properties of zinc(II) complexes in solution and film.

Zinc(II) complexes	Solution		Film			Δ λ_{max} upon film formation
	λ_{max} (nm) (ε_1, × 10^3 $M^{-1}cm^{-1}$, ε_2, × L $g^{-1}cm^{-1}$)	λ_{onset} (nm)	λ_{max} (nm) (Absorption Coefficient α, × 10^5 cm^{-1})	λ_{onset} (nm)	Optical gap (eV)	
$Zn(WS3)_2$	300 (90, 66), 645 (114, 84), 674 (121, 89)	753	701 (2.14)	791	1.57	27
$Zn(L1)_2$	300 (94, 55), 344 (66, 39), 650 (122, 72), 679 (135, 79)	760	716 (2.11)	801	1.55	37
$Zn(L2)_2$	330 (86, 45), 373 (65, 34), 664 (123, 65), 700 (143, 75)	775	727 (2.13)	805	1.54	27

similar to that of $Zn(WS3)_2$, but the visible band is red-shifted by ~5 nm to λ_{max} of 679 nm due to the electron donating hexyl groups, and the absorptivity (ε_1) increases from 1.21×10^5 $M^{-1}cm^{-1}$ at λ_{max} of 674 nm for $Zn(WS3)_2$ to 1.35×10^5 $M^{-1}cm^{-1}$ at λ_{max} of 679 nm for $Zn(L1)_2$. The spectrum of $Zn(L2)_2$ is also similar to $Zn(WS3)_2$ but is further red-shifted to a λ_{max} of 700 nm and the absorptivity of the visible band increases to 1.43×10^5 $M^{-1}cm^{-1}$, most likely due to the larger conjugated length of $Zn(L2)_2$. A similar trend in λ_{max} was observed for the film absorption spectra (Figure S16a), with λ_{max} increasing from 701 nm for $Zn(WS3)_2$ to 716 and 727 nm for $Zn(L1)_2$ and $Zn(L2)_2$, respectively. Absorption coefficients for all zinc complexes were similar, at ~2.1×10^5 cm^{-1} (Table S16b). Table 1 reports the red-shift of the λ_{max} observed upon film formation. All complexes red-shifted upon film formation, suggesting increased intermolecular interactions in the solid state. Interestingly, λ_{max} of $Zn(L1)_2$ red-shifts 37 nm in films compared to 27 nm for both $Zn(WS3)_2$ and $Zn(L2)_2$, suggesting that hexyl groups on the proximal phenyl rings induced more intermolecular interactions in $Zn(L1)_2$. The cyclic voltammograms (CV) of the zinc(II) complexes in dichloromethane are shown in Figure S18 and summarized in Table S1. The CV of PCBM obtained in our laboratory under the same conditions is also included for comparison. The CVs of $Zn(L1)_2$ and $Zn(L2)_2$ are similar to that of $Zn(WS3)_2$, with two reversible oxidation and two reversible reduction peaks. Figure 2b summarizes the estimated HOMO and LUMO energy levels obtained from the $E_{1/2}$ values of the first oxidation and firs reduction peaks, respectively. Both $Zn(L1)_2$ and $Zn(L2)_2$ have very similar LUMO energy levels to $Zn(WS3)_2$, whereas the estimated HOMO levels were a bit higher than $Zn(WS3)_2$, by 0.05 and 0.06 eV for $Zn(L1)_2$ and $Zn(L2)_2$, respectively. These small estimated energy level changes are unlikely to have any significant impact on device performance when using P3HT as the donor.

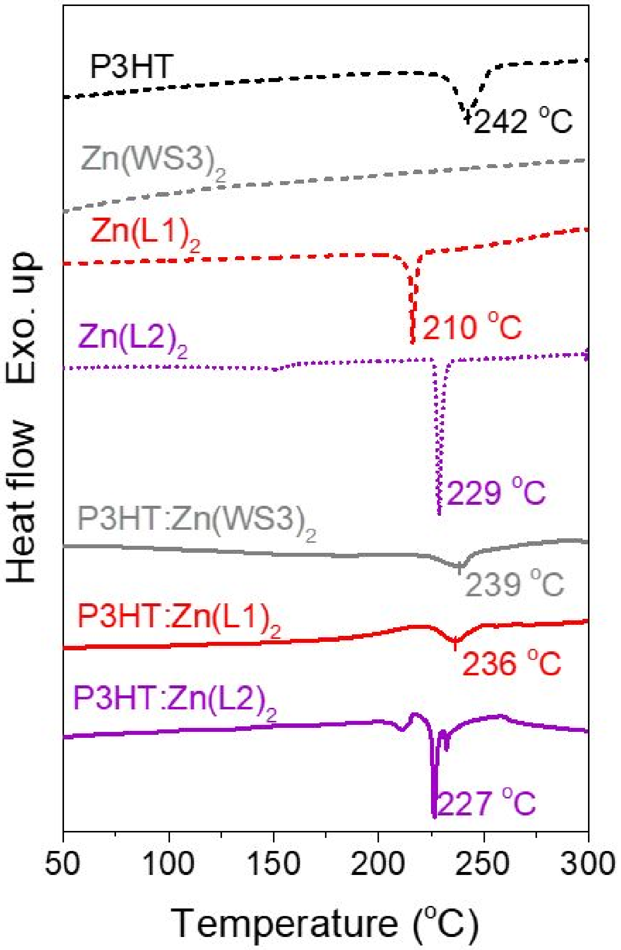

Figure 3. DSC curves for the zinc(II) complexes and P3HT:zinc(II) complexes blends in first heating cycle. The blend ratios are the same as for the optimized ratios in OPVs.

Thermal Properties

The thermal stability of the zinc(II) complexes were investigated by thermal gravimetry analysis (TGA). The thermographs areshown in Figure S17. All zinc(II) complexes were thermally stable, with a 5% weight loss temperature (T5%) of 462, 454 and 415 °C for $Zn(WS3)_2$, $Zn(L1)_2$ and $Zn(L2)_2$, respectively. While the hexyl groups had little impact on the stability of the complexes, the substitution of phenyl with naphthyl groups slightly reduced T5%. Nevertheless, these T5% values are sufficiently high for most device fabrication conditions.

Figure 3 shows the differential scanning calorimetry (DSC) profiles of the first heating cycle for P3HT, zinc(II) complexes, and blends of zinc(II) complexes with P3HT. The first cooling cycle and subsequent heating/cooling cycles are featureless. For neat films, Zn(L1)$_2$ and Zn(L2)$_2$ both showed an exothermic peak during the first heating cycle at 210 °C (enthalpy ΔH_f = 33 J/g) and 229 °C (ΔH_f = 44 J/g), respectively, and no peaks during the cooling cycle. These results are consistent with crystalline Zn(L1)$_2$ and Zn(L2)$_2$ melting into an isotropic liquid upon heating, followed by glass formation upon cooling.[32] Conventional melting point measurements confirmed that the exothermic peak for Zn(L1)$_2$ and Zn(L2)$_2$ is a crystal-melting phase transition (see Figure S19). On the other hand, Zn(WS3)$_2$ exhibits no peaks upon heating and cooling in the 25-300 °C temperature range. This suggests that the hexyl groups increase crystallinity of zinc(II) complexes. The substitution of phenyl groups in Zn(L1)$_2$ with naphthyl groups (Zn(L2)$_2$) further increased crystallinity because the melting temperature and ΔH_f increased by 19 °C and 11 J/g, respectively.

In blend films, a broad exothermic peak in the 235 - 239 °C is assigned to melting of P3HT. These temperatures are slightly lower than the melting temperature of neat P3HT at 242 °C. The calculated ΔH_f for P3HT in neat P3HT, P3HT:Zn(WS3)$_2$, P3HT:Zn(L1)$_2$ and P3HT:Zn(L2)$_2$ are 21, 19, 17, and 17 J/g, respectively. The lower melting temperature and ΔH_f of P3HT in blends indicates that all zinc(II) complexes interfere slightly with P3HT crystallization. In addition, Zn(L2)$_2$ is the only zinc(II) complex that shows a melting transition in blends (at 227 °C), indicating that it is the only complex that remains crystalline in blends with P3HT.

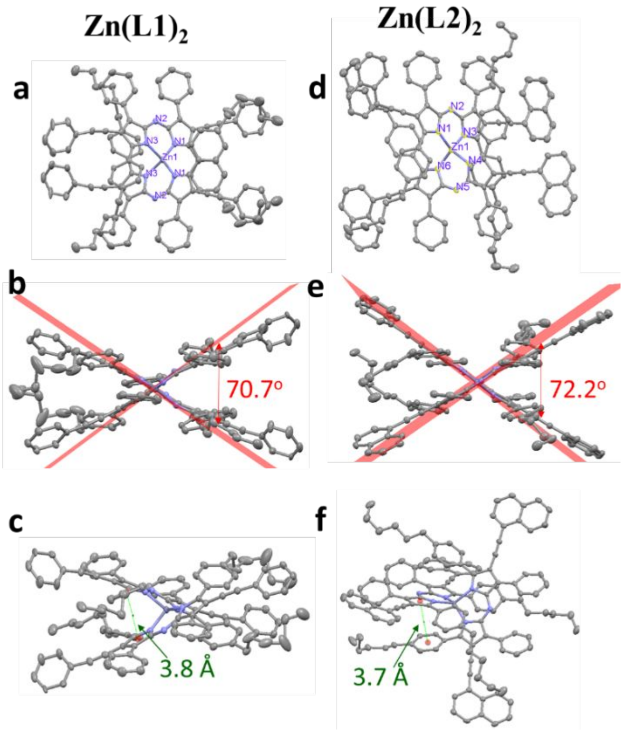

Figure 4. Ellipsoid plot of Zn(L1)$_2$ and Zn(L2)$_2$. The hydrogen atoms, and dichloromethane solvate were omitted for clarity. a) and d) show the structure of Zn(L1)$_2$ and Zn(L2)$_2$, respectively; b) and e) show the distorted tetrahedral shape; c) and f) show the intramolecular π-π stacking between the proximal phenyl group of one ligand and a core (pyrrole ring) of the other ligand. Distance was measured between the centroids of the rings.

Crystallography

Both Zn(L1)$_2$ and Zn(L2)$_2$ were successfully crystalized by dissolving the complexes in a solvent mixture of dichloromethane and acetonitrile with volume ratio of 8:1, followed by slow evaporation of dichloromethane from the mixture. The crystals were large, diamond-shaped and dark purple in color (see Figure S21). On the other hand, multiple attempts to crystalize Zn(WS3)$_2$ only resulted in very small needle-shaped crystals, which were not suitable for single crystal structure determination. Since the only structural difference between Zn(L1)$_2$ and Zn(WS3)$_2$ is the hexyl groups on the proximal phenyls, it is likely that the hexyl groups facilitate the molecular packing and thus crystallization of zinc(II) complexes, consistent with the DSC results above. Without the hexyl groups, Zn(WS3)$_2$ is a good glass-former because it is too rigid to pack into long range order. Figure 4 shows the ellipsoid plot of Zn(L1)$_2$ and Zn(L2)$_2$. Similar to Zn(ADP)$_2$, the zinc(II) complexes exhibit a distorted tetrahedral structure with intra-molecular π-π stacking in four places between a proximal phenyl of one ligand and a pyrrole ring of the other ligand. Zn(L2)$_2$ exhibits a larger dihedral angle, 72.2°, and a smaller intra-molecular π-π stacking distance (3.73 Å) than Zn(L1)$_2$, which has dihedral angle of 70.7° and π-π stacking distance of 3.82 Å. The shorter π-π stacking distance for Zn(L2)$_2$ suggests a stronger intra-molecular interaction between the proximal phenyl and pyrrole rings. Moreover, Zn(L1)$_2$ and Zn(L2)$_2$ show different crystal packing depending on the aryl groups used on the pyrrolic acetylene positions, see Figure S21. Zn(L1)$_2$ has a T-shape inter-molecular interaction between distal and pyrrolic phenyl rings and a parallel interaction between proximal phenyls. On the other hand, Zn(L2)$_2$ prefer a T-shape inter-molecular interaction between the pyrrolic naphthyls and the distal phenyls and another T-shape interaction between the pyrrolic naphthyls and the pyrrole rings in the core. The inter and intra molecular interacting properties of these zinc(II) complexes are summarized in Table 2. This demonstrates that the nature of the aryl group has a strong influence on ligand arrangement and self-assembly in the solid state. In addition, these zinc(II) complexes exhibit 3D π-π interactions in the crystal.

Calculations

The electronic structures of Zn(L1)$_2$ and Zn(L2)$_2$ were investigated with density-functional theory (DFT) calculations. Unconstrained geometry optimizations converged to local minima of the potential energy hypersurfaces, as verified by harmonic vibrational frequency analyses. Calculated metrics are in good agreement with crystallographic values. Average zinc(II)-nitrogen bonds lengths are 1.93 Å (experimental 1.99 Å) for Zn(L1)$_2$ and 2.01 Å (experimental 2.01 Å) for Zn(L2)$_2$. A noteworthy feature of the structure of each complex is the distorted tetrahedral geometry about zinc(II). For Zn(L1)$_2$, the computed angle between chelate N–Zn–N planes is 84.4° (75.3°, experimental); for Zn(L2)$_2$, this angle is 85.1° (74.8°, experimental). Thus, gas-phase geometry optimizations capture

Table 2. Summary of inter- and intra- molecular interactions of zinc(II) complexes.

Zn complexes	Intramol. dihedral angle (°)	Intramol. π-π stacking distance (Å)	Intermol. π-π stacking type	Intermol. π-π stacking distance (Å)
$Zn(L1)_2$	70.7	3.82	Distal-Pyrrolic (T) and Proximal-Proximal (P)	4.34, 4.83
$Zn(L2)_2$	72.2	3.73	Pyrrolic-Core (T) and Pyrrolic-Distal (T)	4.78, 4.42

Note: Distal, proximal, pyrrolic and core mean the distal phenyl ring, proximal phenyl ring, pyrrolic phenyl ring and pyrrole ring, respectively. Intermolecular π-π stacking types are sandwich (S), T-shaped (T) and parallel (P) π-π stacking.

the flattened structure of the complexes, despite the absence of ligand-field stabilization for zinc(II) (d10).

Figure 5 shows the contour plots of four frontier orbitals of $Zn(L1)_2$. The two highest occupied Kohn-Sham orbitals (HOMOs) are quasi-degenerate, as are the first two lowest unoccupied Kohn-Sham orbitals (LUMOs). All four orbitals are delocalized over both ligands, with minimal participation of zinc(II). For both HOMOs and both LUMOs, the greater part of each orbitals resides on the tetraphenyl azadipyrromethene moiety, and contributions from the arylalkynyl substituents are substantial. The n-hexyl substituents participate negligibly. Similar results are observed from the frontier orbitals of $Zn(L2)_2$, see Figure S22.

Time-dependent DFT calculations were performed on the first 40 Franck-Condon singlet states of both complexes. The low-energy absorption spectra of $Zn(L1)_2$ and $Zn(L2)_2$ can be rationalized in terms of a four-orbital model involving single-particle excitations from the two HOMOs to the two LUMOs. Figure 6 is a state diagram depicting the relevant transitions for $Zn(L1)_2$. All four transitions in the figure engage in configuration interaction; the figure indicates the major contributors to each state. The first two Frank-Condon singlets have minuscule oscillator strengths, 0.018 and 0.016, respectively, for $Zn(L1)_2$. These transitions contribute sparingly to the absorption onset. Oscillator strengths of the third and fourth transitions are much higher, 0.88 and 1.2 respectively. Together, these transitions account for the major absorptions at 650 and 679 nm for $Zn(L1)_2$, and for the complex's intense blue color. Similar results occur for $Zn(L2)_2$, and a four-state diagram is reproduced as Figure S23. These results parallel earlier calculations on bis(azadipyrromethenes) of zinc(II),[33] and mono(azadipyrromethene) complexes of other d10 metal ions.[34-36] The changes in orbital compositions between the two highest occupied and two lowest unoccupied orbitals (indicated in Figure 5) suggest a degree of charge transfer from the alkynyls to the azadipyrromethene in these intra-ligand π-π* transitions.

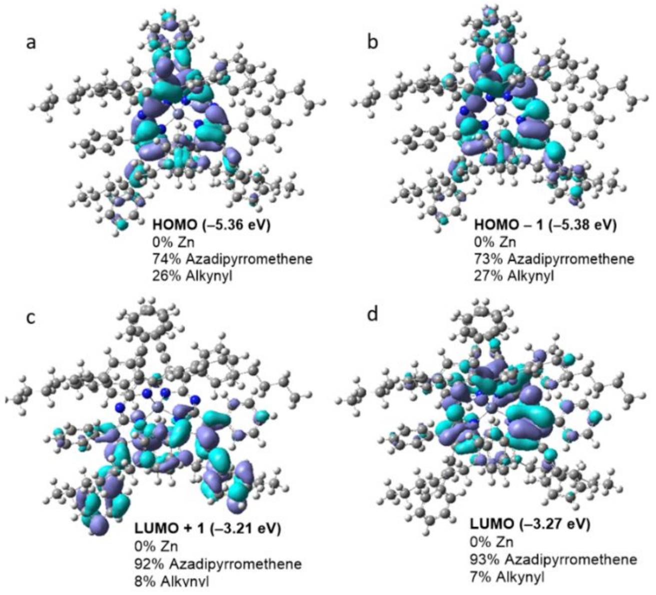

Figure 5. Plots of the a) HOMO, b) HOMO – 1, c) LUMO + 1 and d) LUMO of $Zn(L1)_2$ (contour level 0.02 a.u.). Orbital compositions are expressed as percentages of electron density.

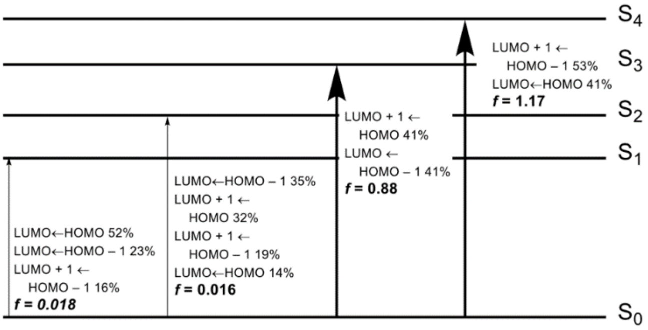

Figure 6. Lowest-lying Franck-Condon singlet excited states of $Zn(L1)_2$ (energies not shown to scale). Percentage composition of vertical transitions and oscillator strengths are indicated to the right of each arrow.

Photovoltaic properties

Photovoltaic properties were investigated using an inverted configuration: ITO/ZnO/P3HT:acceptor/MoO_3/Ag. Device processing optimization involved screening for donor-to-acceptor blend weight ratios, total concentration, and annealing conditions; optimization details are summarized in Table S2-8. Figure 7a shows the current density - voltage curves of the best devices, and the performance parameters are summarized in Table 3. The best PCE obtained were 2.5%, 3.0% and 5.5% for $Zn(WS3)_2$, $Zn(L1)_2$ and $Zn(L2)_2$, respectively. The 5.5% PCE for the $Zn(L2)_2$ cell is amongst the best reported performances for P3HT-based OPV, due to its high V_{OC}, J_{SC} and FF being 0.83V, 11.3 mA/cm^2 and 59%, respectively. In addition, $Zn(L2)_2$ cell performance was much less sensitive to the donor:acceptor ratio than for other zinc(II) complexes: for example, PCE of $Zn(L2)_2$ cells ranged between 4.1% and 5.4% for ratios of 1:0.5 to 1:1.5 (Table S5), whereas PCE of $Zn(L1)_2$ ranged between 1.4% and 2.4% for ratios of 1:0.6 to 1:1.1 (Table S2).

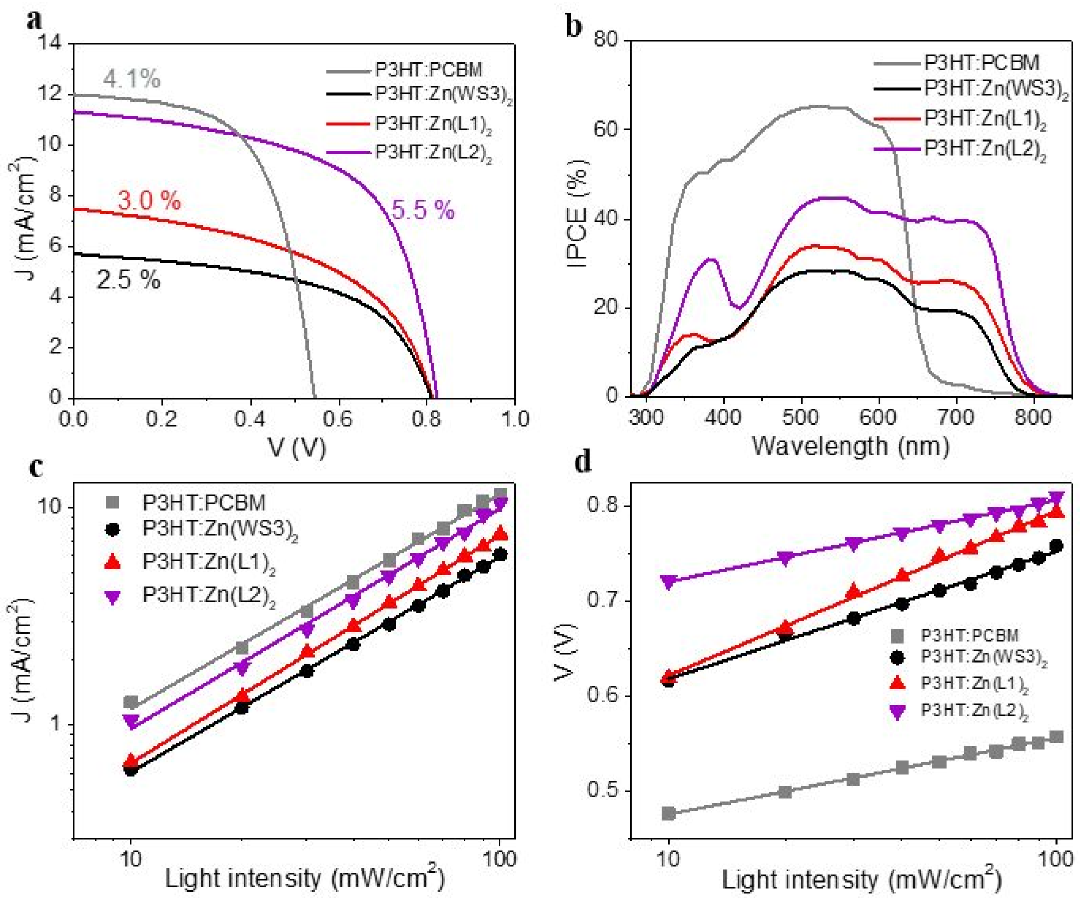

Figure 7. a) Current density–voltage characteristics of solar cells with effective area of 0.2 cm^2 by using simulated AM1.5G illumination at 100 mW/cm^2; b) Incident photon-to-current efficiency (IPCE) spectra of solar cells. c) J_{SC} as a function of light intensity in a double-logarithmic scale and d) V_{OC} as a function of light intensity in a semi-logarithmic scale. Fill factor for all cells did not change much in the light intensity ranging from 10 to 100 mW/cm^2.

The low sensitivity of Zn(L2)$_2$ performance with the donor:acceptor ratio should be advantageous for commercialization.

To better understand the PCE differences, we analyzed the device performance parameters. All zinc(II) complex cells have higher open-circuit voltages (V_{OC}, ~0.8V) than the reference PCBM cell (0.54V), partly due to the higher LUMO energy level of the zinc(II) complexes. The V_{OC} difference was higher than the difference between the Zn complexes and PCBM energy levels, suggesting that there is less energy losses in the non-fullerene cells. More accurate determination of the LUMO energy levels in films is required to confirm this. The short circuit current (J_{SC}) increased with the introduction of hexyl groups from 5.7 mA/cm^2 for Zn(WS3)$_2$ to 7.5 mA/cm^2 for Zn(L1)$_2$. Replacing the pyrrolic phenyls with naphthyls further increased J_{SC} to 11.3 mA/cm^2 for Zn(L2)$_2$. These J_{SC} increases cannot be explained by increased absorption alone. Figure S24 shows the UV-Vis absorption of P3HT:zinc(II) complexes blend films made under the same optimized conditions than the active layer in solar cells. All zinc(II) complex blends have a similar absorbance between 450 nm and 800 nm. Although the P3HT:Zn(L2)$_2$ films exhibit a slightly larger absorption in the 640 nm – 800 nm region, it is not sufficient to explain the large J_{SC} increase. The J_{SC} increases are consistent with increases in the incident photon-to-current efficiencies (IPCEs, Figure 7b): IPCE at 510 nm was 28%, 34% and 44% for Zn(WS3)$_2$, Zn(L1)$_2$ and Zn(L2)$_2$, respectively. The J_{SC} of Zn(L2)$_2$ cell calculated by integrating the IPCE spectra was 9.9 mA/ cm^2, which is 12% lower from the measured J_{SC}. This small difference may be due to cell degradation, as the IPCE measurements were done in air instead of in the glove box. The maximum IPCEs for the zinc(II) complex cells are generally lower than for PCBM cells because the optimized cell thickness of the zinc(II) complex cells is thinner, ~80 nm, than that of the PCBM cell, ~190 nm, thus limiting absorption for the zinc(II) complexes cells. The J_{SC} and IPCE trends observed within the zinc(II) complex series cannot be explained from absorption differences alone, and must depend on other factors affecting photocurrent such as exciton splitting, free charge generation and charge carrier recombination.

To further understand the OPV results, charge recombination was investigated from J-V light intensity dependence measurements. Figure 7c shows the J_{SC} as a function of light intensity in a double-logarithmic scale and the extracted power law exponent for all solar cells are reported in Table 3. All power law exponents were close to unity, indicating that the loss from bimolecular recombination in all optimized cells is small.[37] Figure 7d shows the V_{OC} as a function of light intensity in a semi-logarithmic scale. There is a monotonic relationship between V_{OC} and light intensity. The data were

Table 3. Performance parameters, power law exponents and V_{oc} slopes of solar cells.

Acceptor	V_{OC}(V)	J_{SC} (mA cm^{-2})	FF (%)	PCE (%)	Power law exponent	V_{OC} slope (Times of kT/q)
Zn(WS3)$_2$	0.81 (0.77 ± 0.03) [a]	5.7 (5.4 ± 0.7) [a]	55 (52 ± 6) [a]	2.5 (2.1 ± 0.4) [a]	0.990	2.6
Zn(L1)$_2$	0.81 (0.80 ± 0.03)	7.5 (7.3 ± 0.3)	49 (49 ± 2)	3.0 (2.8 ± 0.2)	1.05	2.0
Zn(L2)$_2$	0.82 (0.82 ± 0.01)	11.3 (10.8 ± 0.7)	59 (59 ± 3)	5.5 (5.2 ± 0.3)	1.01	1.3
PCBM	0.54 (0.54 ± 0.02)	12.0 (11.5 ± 0.6)	63 (63 ± 1)	4.1 (4.0 ± 0.2)	0.988	1.2

Note: For solar cells, all acceptors were tested by blending with P3HT using optimized conditions. Averages were calculated for at least 10 devices. k is Boltzmann's constant, T is temperature, and q is elementary charge.

Table 4. Charge carrier mobility of zinc(II) complexes by using SCLC and TFT methods.

Acceptor	Mobility measured by SCLC				Mobility measured by TFT	
	Neat μ_h (cm^2 V^{-1} s^{-1})	Neat μ_e (cm^2 V^{-1} s^{-1})	Blend μ_h (cm^2 V^{-1} s^{-1})	Blend μ_e (cm^2 V^{-1} s^{-1})	Neat μ_h (cm^2 V^{-1} s^{-1})	Neat μ_e (cm^2 V^{-1} s^{-1})
Zn(WS3)$_2$	8.1×10^{-7}	1.6×10^{-5}	2.4×10^{-4}	4.0×10^{-6}	--	2.3×10^{-5}
Zn(L1)$_2$	9.0×10^{-7}	3.2×10^{-5}	3.0×10^{-4}	4.0×10^{-5}	--	4.6×10^{-5}
Zn(L2)$_2$	1.0×10^{-4}	4.2×10^{-5}	3.1×10^{-4}	2.4×10^{-5}	1.3×10^{-4}	6.8×10^{-5}
PCBM	--	5.0×10^{-3} [a]	5.5×10^{-4} [a]	2.6×10^{-3} [a]	--	--

Note: A minimum of 4 devices were made for each mobility measurement and average values are reported. Blend mobilities were measured from blends of acceptors and P3HT using the same fabrication method as optimized solar cells. [a] Published data.[26]

fitted into a linear function and the extracted slopes, presented as multiples of kT/q, are summarized in Table 3. A slope of one kT/q indicates that only Langevin recombination is present and a higher than kT/q slope means trap assisted recombination is also present.[37-38] The slope for P3HT:PCBM cells, 1.2 kT/q, is close to the reported data, 1.4 kT/q, for P3HT:PCBM cells under similar fabrication conditions.[39] Since PCBM is a trap-free material, the carrier traps in P3HT:PCBM cell was mainly induced by P3HT.[40] The slope for Zn(WS3)$_2$, Zn(L1)$_2$, and Zn(L2)$_2$ cells are 2.6, 2.0 and 1.3 times kT/q, respectively, indicating Zn(WS3)$_2$ has the largest loss from trap assisted recombination, followed by Zn(L1)$_2$ and Zn(L2)$_2$. This is also consistent with the J_{SC} and PCE trends in OPVs, and partially explains the high J_{SC} and high fill factor in Zn(L2)$_2$ cells.[39] The slope of Zn(L2)$_2$ cell, 1.3 kT/q, is very close to that of PCBM cell, 1.2 kT/q, suggesting that the carrier traps are mainly induced by P3HT, and that Zn(L2)$_2$ may be nearly trap free.

Charge transport properties

To further understand the performance of zinc(II) complex devices, space-charge-limited-current (SCLC) method was used to measure charge carrier mobilities of zinc(II) complexes in neat and blend films. Hole mobility (μ_h) measurement used a device structure of ITO/PEDTO:PSS/active layer/MoO$_3$/Ag and electron mobility (μ_e) measurement used a device structure of ITO/ZnO/active layer/Ca/Al. Mobilities were calculated with the Mott-Gurney law under the trap free SCLCs situation.[41] The SCLC graphs are shown in Figure S25 and the results are summarized in Table 4. The film electron mobility of all neat zinc(II) complexes varied slightly within the same magnitude, ranging from 1.6×10^{-5} to 4.2×10^{-5} cm^2 V^{-1} s^{-1}, which are about an order of magnitude lower than that of high efficiency NFAs. The relatively low electron mobility of zinc(II) complexes limits the film thickness of optimized cells to ~80 nm, thus limiting light absorption and J_{SC} in cells. Interestingly, both Zn(L1)$_2$ and Zn(WS3)$_2$ have similar neat film hole mobility, around 9×10^{-7} cm^2 V^{-1} s^{-1}. This is about two orders of magnitude lower than that of Zn(L2)$_2$, 1.0×10^{-4} cm^2 V^{-1} s^{-1}, which is close to the reported hole molibility of pristine P3HT film, $(1.4 - 3) \times 10^{-4}$ cm^2 V^{-1} s^{-1}.[42] This indicates that Zn(L2)$_2$ can not only transport electrons, but the favorable intermolecular interaction in Zn(L2)$_2$ also facilitates hole transport in the neat film. Blend film mobilities of zinc(II) complexes were also studied. After blending with P3HT, $Zn(WS3)_2$ had a one magnitude drop in electron mobility, from 1.6×10^{-5} $cm^2\ V^{-1}\ s^{-1}$ in neat film to 4.0×10^{-6} $cm^2\ V^{-1}\ s^{-1}$ in blend film. In contrast, for $Zn(L1)_2$ and $Zn(L2)_2$ electron mobility in blends was similar than in neat films. This suggests that the hexyl chains help the zinc(II) complexes maintain a favorable phase separation from P3HT to maintain good electron transport in blends. The hole mobility for all P3HT:zinc(II) complex blends was ~ 3×10^{-4} $cm^2\ V^{-1}\ s^{-1}$, attributed to the hole transport in P3HT. The imbalance between electron and hole mobility may also contribute to charge recombination and low FF.

The SCLC method provides insight into the out-of-plane charge transport between the two electrodes. To investigate in-plane charge transport along the substrate, charge transport in bottom-gate-bottom-contact thin film transistors (TFT) were measured, see Table 4. The electron mobility was estimated to be 2.3×10^{-5}, 4.6×10^{-5}, and 6.8×10^{-5} $cm^2\ V^{-1}\ s^{-1}$ for $Zn(WS3)_2$, $Zn(L1)_2$ and $Zn(L2)_2$, respectively. These numbers are similar to those obtained in neat films by SCLC method. This suggests that charge transport is similar in the two directions in the film, and is consistent with our hypothesis that the 3D π-π stacking of zinc(II) complexes enable isotropic charge transport. Hole mobility of $Zn(L2)_2$ films was 1.3×10^{-4} $cm^2\ V^{-1}\ s^{-1}$ in TFTs, very similar to the value of 1.0×10^{-4} $cm^2\ V^{-1}\ s^{-1}$ obtained by SCLC method, also consistent with isotropic charge transport.

Morphology

The surface morphology of the optimized cell films (annealed) was studied by tapping-mode atomic force microscopy (AFM). The phase and height images for all zinc(II) complex cells are shown in Figure 8. The height images show that the films are smooth, with surface roughness ranging from 12 to 5 nm. The phase images show more defined features, with lighter and darker parts related to domains having different adhesion and mechanical properties.[43] The two materials appear to be phase separated with irregular shaped domains of 25 to 50 nm for P3HT:$Zn(WS3)_2$ and P3HT:$Zn(L1)_2$ blends, and 15 to 40 nm for the P3HT:$Zn(L2)_2$ blends. This phase separation should be good for charge transport to electrodes, consistent with the low bimolecular recombination observed. The smaller domain size range observed for the P3HT:$Zn(L2)_2$ blends are expected to be more favorable for exciton splitting and charge generation than the domain size range of the other two blends. The P3HT:$Zn(L2)_2$ blend therefore appears to have the best surface morphology among the three blends, having small enough phase-separated domains for exciton splitting and large enough phase-separated domains for good charge transport to the electrodes.[44]

To gain insight about crystalline structure and crystal orientation across the films, neat and blend films were analyzed by two-dimensional (2D) grazing-incidence wide-angle X-ray diffraction (GI-WAXD). The 2D GI-WAXD patterns and corresponding intensity profiles along the q_r (in-plane) direction of the annealed films are shown in Figure 9, and those for the as-cast films can be found in Figure S30. Both as-cast neat films of $Zn(L1)_2$ and $Zn(L2)_2$ were amorphous. Upon annealing, $Zn(L1)_2$ remained amorphous whereas $Zn(L2)_2$ crystallized. The GI-WAXD pattern of the annealed $Zn(L2)_2$ film shows four defined out-of-plane peaks at $q_z \approx 0.40$, 0.52, 0.63, and 0.71 $Å^{-1}$, and two defined in-plane peak at $q_r \approx 1.47$ and 1.52 $Å^{-1}$. These matched well with diffractions in the powder pattern calculated from the single crystals, as labeled in the Figure S29. The annealed P3HT:$Zn(L1)_2$ blend film shows three orders of out-of-plane (100) lamellar peaks, at $q_z \approx 0.40$, 0.79, and 1.21 $Å^{-1}$, corresponding to the edge-on orientation of P3HT. An in-plane π-π stacking reflection, (010), was also found at $q_r \approx 1.69$ $Å^{-1}$, which is consistent with the P3HT crystal structure.[45] This suggests that only P3HT is crystalline in the P3HT:$Zn(L1)_2$ blend films, consistent with the DSC data. The annealed P3HT:$Zn(L2)_2$ blend film shows the P3HT diffraction pattern, indicating the crystallinity of P3HT was maintained in the blend film. In addition, two defined in-plane diffraction peaks at $q_r \approx 0.52$ and 1.52 $Å^{-1}$ indicated molecular ordering of $Zn(L2)_2$, consistent with the DSC result that both $Zn(L2)_2$ and P3HT are crystalline in the blend film.

To estimate the crystallite size of P3HT and $Zn(L2)_2$, the GI-WAXD data was analyzed using the Scherrer equation:[46-47]

$$\tau_{hkl} = \lambda \times 0.9/(\beta \cos\theta) \qquad \text{Equation (3)}$$

Where τ_{hkl} is the crystallite size along the [hkl] reflection, λ is the X-ray wavelength and β is the full width at half maximum of the

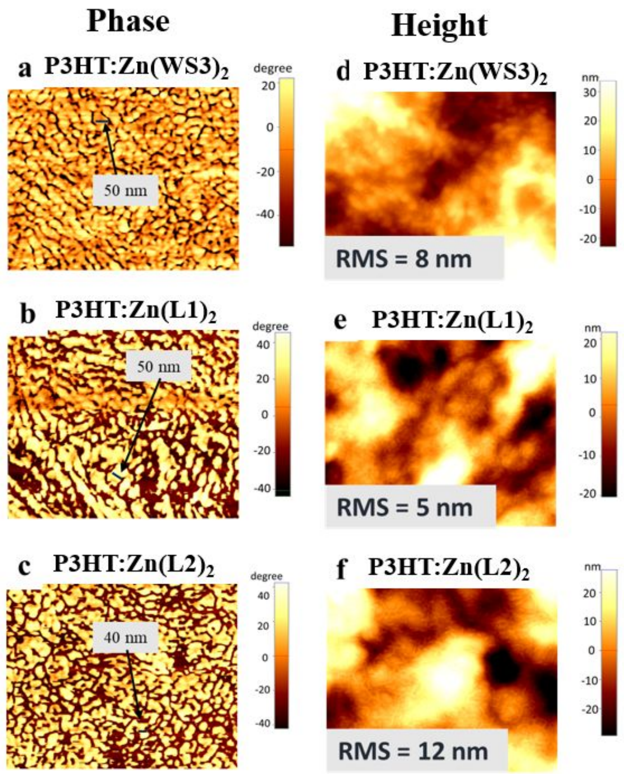

Figure 8. a), b), c) phase images for the optimized OPV films of P3HT:$Zn(WS3)_2$, P3HT:$Zn(L1)_2$ and P3HT:$Zn(L2)_2$, respectively; d), e), f) height images for P3HT:$Zn(WS3)_2$, P3HT:$Zn(L1)_2$ and P3HT:$Zn(L2)_2$ films respectively. In phase images, dark and bright parts can be differentiated as different components. All films were annealed at same conditions to optimized OPVs and all images are 1×1 μm^2.

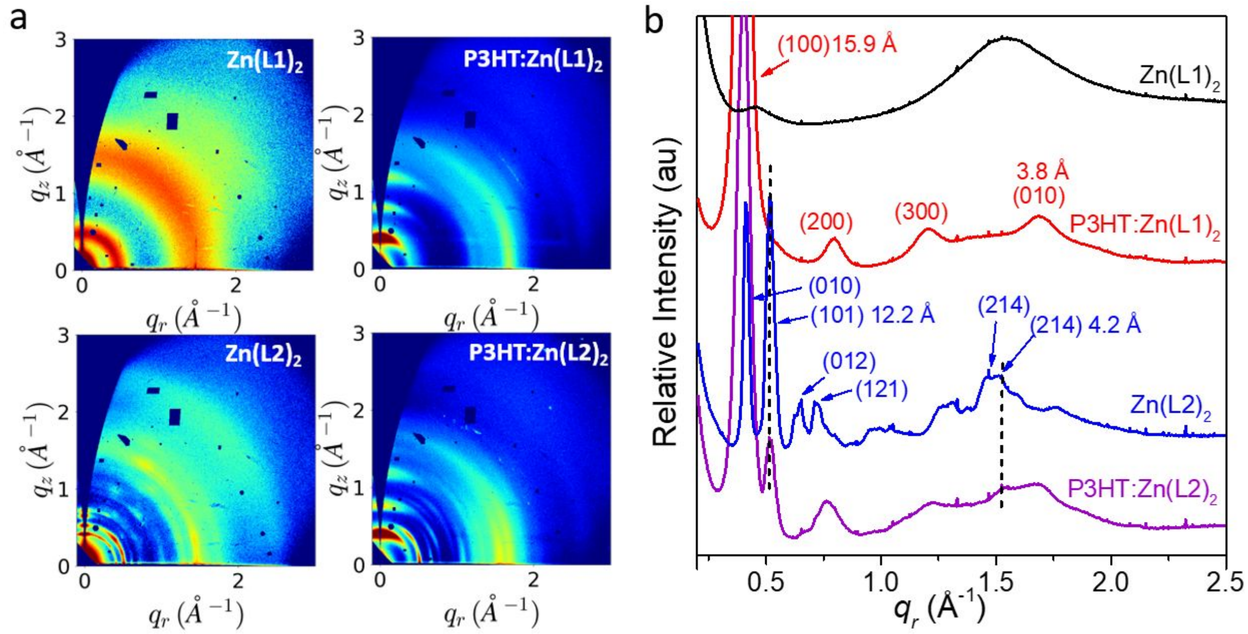

Figure 9. a) 2D GI-WAXD patterns of thermally annealed thin films of Zn(L1)$_2$, Zn(L2)$_2$, P3HT:Zn(L1)$_2$ and P3HT:Zn(L2)$_2$. The *r* and *z* directions indicate in-plane and out-of-plane directions. The Zn(L1)$_2$ neat and blend films were annealed at 100 °C for 15 min and the Zn(L2)$_2$ films were annealed at 120 °C for 15 min. b) Corresponding intensity profiles along the q_r axis.

diffraction peak. The diffraction patterns of P3HT and Zn(L2)$_2$ are shown in Figure S31. In annealed neat films, the τ_{001} of P3HT and τ_{101} of Zn(L2)$_2$ were estimated to be 12.5 and 13.7 nm, respectively. In P3HT:Zn(L2)$_2$ annealed blend film, the crystallite size of P3HT decreased slightly to 8.7 nm due to the presence of Zn(L2)$_2$. However, the crystallite size of Zn(L2)$_2$ remained similar in both neat and blend films, at 13.7 nm and 12.3 nm, respectively. These crystallite sizes are favorable for efficient exciton splitting, in agreement with the AFM data presented above.

Donor Properties of Zn(L2)$_2$ in OPVs

The SCLC and TFT measurements show that Zn(L2)$_2$ is ambipolar with a well-balanced electron and hole mobility (both electron mobility and hole mobility at around 1 × 10^{-4} cm^2 V^{-1} s^{-1}). To investigate the electron donating property of Zn(L2)$_2$ in OPVs, we first attempted to blend Zn(L2)$_2$ with PCBM, but this resulted in uneven films, possibly because both are small molecules with non-planar shape. To improve film quality, we then turned to a polymer acceptor that we had available in our laboratory: Poly{[*N*,*N*′-bis(2-octyldodecyl)-naphthalene-1,4,5,8-bis(dicarboximide)-2,6-diyl]-*alt*-5,5′-(2,2′-bithiophene)} (P(NDI2OD-T2)) from Polyera. The estimated energy levels for this polymer are lower than Zn(L2)$_2$, though the energy offsets are small and not optimal, at ~0.2 and 0.1 eV for LUMOs and HOMOs, respectively (see Figure S32). Nevertheless, we fabricated OPVs using the unoptimized conditions; 1:1 weight ratio with a total concentration of 25 mg/mL in *o*-DCB, annealed at 80°C for 15 min. Preliminary results show a photovoltaic effect with a J_{SC} of 0.084 mA/cm^2, a V_{OC} of 0.86 V, a FF of 37% and a PCE of 0.027% (Figure S32), demonstrating that Zn(L2)$_2$ has potential as donor in OPVs. We note that other azadipyrromethene-based dyes have been reported to work as donor with evaporated fullerene (C$_{60}$) as the acceptor.[48-50] Since morphology is critical for good performance, the surface morphology of the blend films was imaged by AFM, Figure S28. The domain size appears to be ~12 nm, and the film has a surface roughness of 2.8 nm, with no obvious large-scale phase separation. The low performance is likely due to a combination of unoptimized energy level alignment (See Figure S32), non-complementary absorption of the two components (both absorb in UV and between 600-800 nm), and low exciton diffusion length of P(NDI2OD-T2) (1.1 nm, much smaller than the 12 nm domain size observed).[51] The 3-D molecular shape and good hole mobility of Zn(L2)$_2$ is expected to enable high performance with a high bandgap polymer acceptor that has a deep LUMO energy level – however, optimization of the polymer acceptor is required and is beyond the scope of this paper.

Commercial accessibility of P3HT:Zn(L2)$_2$ cells

The synthetic complexity (SC) for Zn(L1)$_2$ and Zn(L2)$_2$ was evaluated by considering the number of synthetic steps, yields, number of purification steps, purifications by column chromatography and number of hazardous chemicals. Details are given in the Supporting Information section. The SC index was calculated to be 22.9 and 22.1% for Zn(L1)$_2$ and Zn(L2)$_2$, respectively, Table S10 and S11. These numbers are close to PCBM (20.6%) and lower than the low-cost NFAs such as MO-IDIC-2F (25.2%, Table S11) and high performance NFAs such as O-IDTBR (43.9%).[523] Figure S33 shows the normalized photostability of P3HT:Zn(L2)$_2$ cells in air and under N$_2$. After 200 h of illumination, the photostability was 81% and 74% in N$_2$ atmosphere and in air, respectively. The industrial figure of merit, i-FoM, was calculated from the PCE, photostability under N$_2$ and SC of the blend.[23] For P3HT:Zn(L2)$_2$, PCE is 5.5%, photostability is 0.81 and the SC for the blend is 15%, giving an i-FoM value of 0.30, which is one of the highest i-FoM reported to date.[23] The i-FoM of the PTQ10-MO-IDIC-2F system has not been reported to our knowledge. Assume a good photostability of 0.8, we estimate an i-FoM value of 0.5, higher than our system due to the higher PCE. To increase the commercial accessibility of $Zn(L2)_2$-based solar cells, it is therefore critical to further improve PCE.

Conclusions

Two zinc(II) ADP complexes, $Zn(L1)_2$ and $Zn(L2)_2$, have been successfully synthesized through functionalization of $Zn(WS3)_2$. Both hexyl groups and substitution of phenylethynyl with naphthylethynyl improve crystallinity of the zinc(II) complexes. Density-functional theory calculations find that the frontier orbitals extend over the azadipyrromethene chromophore and the arylalkynyl substituents, with minimal involvement of zinc. Time-dependent DFT calculations indicate that the complexes' absorption of low-energy visible light results from four ligand-centered π-π* states, where the alkynyl moieties act as electron donors to the azadipyrromethene core. XRD structure shows intermolecular interactions in 3 dimensions and mobility measurements in both diode and transistor geometry demonstrate that charge transport is isotropic and ambipolar. $Zn(L1)_2$ and $Zn(L2)_2$ were tested in OPVs using P3HT as donor and a PCE of 5.5% was obtained for $Zn(L2)_2$. The improved efficiency compared to $Zn(WS3)_2$ was explained by the improved electron mobility in blend films, good crystallinities of $Zn(L2)_2$ and P3HT, proper nanoscale phase separation and relatively low trap-assisted recombination. Compared to higher efficiency systems, the electron mobility of $Zn(L2)_2$ is relatively low, limiting film thickness, photocurrent and FF. We are exploring other molecular modifications to increase electron mobility. Further studies are required to better understand charge separation efficiency in these systems. Finally, we will explore using other simple polymer donors with demonstrated higher efficiency than P3HT, such as PTQ10 and poly[(4,4′-bis(2-butyloctoxycarbonyl- [2,2′ -bithiophene]-5,5-diyl)-alt-(2,2′ -bithiophene-5,5′ -diyl)] (PDCBT, where hexyl group of P3HT is replaced with an alkoxycarbonyl, SC=25% in Table S11).[52-54] $Zn(L2)_2$ was also found to have isotropic charge transport with high hole mobility. The electron donating property of $Zn(L2)_2$ in a solar cell was demonstrated, making it a good candidate to pair with wide bandgap polymer electron acceptors with deep LUMO energy levels. The low synthetic complexity and industrial accessibility of $Zn(L2)_2$ have been demonstrated, showing that ADP-based zinc(II) complexes are an excellent platform to develop materials for OPVs.

Acknowledgements

We are grateful to the National Science Foundation (CHEM 1148652) for partially funding this project. We thank Polyera Corporation for providing the polymer P(NDI2OD-T2), Muyuan Zhao for help with the device optimization, Dr. John D. Protasiewicz access to cyclic voltammetry instrumentation, and the Materials for Optoelectronics Research and Education (MORE) Center at CWRU for device fabrication and characterization. We thank Prof. Advincula at CWRU for access to his AFM instruments. This project was possible thanks NSF MRI-0821515 for MALDI-TOF-TOF instrumentation and NSF MRI-1334048 for NMR instrumentation. This research utilized the 11-BM CMS beamline of National Synchrotron Light Source-II (NSLS-II), Brookhaven National Laboratory (BNL), a U.S. Department of Energy User Facility operated for the Office of Science by BNL under contract No. DE-SC0012704. Computations at CWRU were supported by the U.S. Department of Energy, Office of Basic Energy Sciences, Division of Materials Science and Engineering, under Award DE-SC0010714 to T. G. G. This work made use of the High Performance Computing Resource in the Core Facility for Advanced Research Computing at CWRU.

Conflict of Interest

The authors declare no conflict of interest.

Keywords

organic solar cell, low-cost, isotropic charge transport, nonfullerene, additive-free

References

1 G. Zhang,J. Zhao,P. C. Y. Chow,K. Jiang,J. Zhang,Z. Zhu,J. Zhang,F. Huang,H. Yan, *Chem. Rev.,* 2018, **118**, 3447-3507.
2 R. Xue,J. Zhang,Y. Li,Y. Li, *Small,* 2018, **14**, e1801793.
3 R. C. Chiechi,R. W. A. Havenith,J. C. Hummelen,L. J. A. Koster,M. A. Loi, *Mater. Today (Oxford, U. K.),* 2013, **16**, 281-289.
4 Y. Cui,H. Yao,J. Zhang,T. Zhang,Y. Wang,L. Hong,K. Xian,B. Xu,S. Zhang,J. Peng,Z. Wei,F. Gao,J. Hou, *Nat. Commun.,* 2019, **10**, 2515.
5 X. Li,F. Pan,C. Sun,M. Zhang,Z. Wang,J. Du,J. Wang,M. Xiao,L. Xue,Z.-G. Zhang,C. Zhang,F. Liu,Y. Li, *Nat. Commun.,* 2019, **10**, 1-11.
6 J. Yuan,T. Huang,P. Cheng,Y. Zou,H. Zhang,J. L. Yang,S. Y. Chang,Z. Zhang,W. Huang,R. Wang,D. Meng,F. Gao,Y. Yang, *Nat. Commun.,* 2019, **10**, 570.
7 K. Gao,S. B. Jo,X. Shi,L. Nian,M. Zhang,Y. Kan,F. Lin,B. Kan,B. Xu,Q. Rong,L. Shui,F. Liu,X. Peng,G. Zhou,Y. Cao,A. K. Jen, *Adv. Mater.,* 2019, **31**, e1807842.
8 J.-L. Wang,K.-K. Liu,L. Hong,G.-Y. Ge,C. Zhang,J. Hou, *ACS Energy Lett.,* 2018, **3**, 2967-2976.
9 W. Zhao,S. Li,H. Yao,S. Zhang,Y. Zhang,B. Yang,J. Hou, *J. Am. Chem. Soc.,* 2017, **139**, 7148-7151.
10 J. Yuan,Y. Zhang,L. Zhou,G. Zhang,H.-L. Yip,T.-K. Lau,X. Lu,C. Zhu,H. Peng,P. A. Johnson,M. Leclerc,Y. Cao,J. Ulanski,Y. Li,Y. Zou, *Joule,* 2019, **3**, 1140-1151.
11 S. P. Singh,Suman, *J. Mater. Chem. A,* 2019, Ahead of Print.
12 D. Rodriquez,S. Savagatrup,E. Valle,C. M. Proctor,C. McDowell,G. C. Bazan,T. Q. Nguyen,D. J. Lipomi, *ACS Appl. Mater. Interfaces,* 2016, **8**, 11649-11657.
13 S. Holliday,R. S. Ashraf,A. Wadsworth,D. Baran,S. A. Yousaf,C. B. Nielsen,C.-H. Tan,S. D. Dimitrov,Z. Shang,N. Gasparini,M. Alamoudi,F. Laquai,C. J. Brabec,A. Salleo,J. R. Durrant,I. McCulloch, *Nat. Commun.,* 2016, **7**, 11585.
14 W. Zhao,D. Qian,S. Zhang,S. Li,O. Inganas,F. Gao,J. Hou, *Adv. Mater.,* 2016, **28**, 4734-4739.

15 E. Y. Ko,G. E. Park,J. H. Lee,H. J. Kim,D. H. Lee,H. Ahn,M. A. Uddin,H. Y. Woo,M. J. Cho,D. H. Choi, *ACS Appl. Mater. Interfaces,* 2017, **9**, 8838-8847.

16 X. Du,T. Heumueller,W. Gruber,A. Classen,T. Unruh,N. Li,C. J. Brabec, *Joule,* 2019, **3**, 215-226.

17 R. Po,A. Bernardi,A. Calabrese,C. Carbonera,G. Corso,A. Pellegrino, *Energy Environ. Sci.,* 2014, **7**, 925-943.

18 R. Po,G. Bianchi,C. Carbonera,A. Pellegrino, *Macromolecules,* 2015, **48**, 453-461.

19 R. Po,J. Roncali, *J. Mater. Chem. C,* 2016, **4**, 3677-3685.

20 J. Min,Y. N. Luponosov,C. Cui,B. Kan,H. Chen,X. Wan,Y. Chen,S. A. Ponomarenko,Y. Li,C. J. Brabec, *Adv. Energy Mater.,* 2017, **7**, 1700465.

21 R. Lenaerts,T. Cardeynaels,I. Sudakov,J. Kesters,P. Verstappen,J. Manca,B. Champagne,L. Lutsen,D. Vanderzande,K. Vandewal,E. Goovaerts,W. Maes, *Sol. Energy Mater. Sol. Cells,* 2019, **196**, 178-184.

22 C. Sun,F. Pan,H. Bin,J. Zhang,L. Xue,B. Qiu,Z. Wei,Z. G. Zhang,Y. Li, *Nat. Commun.,* 2018, **9**, 743.

23 N. Li,I. McCulloch,C. J. Brabec, *Energy Environ. Sci.,* 2018, **11**, 1355-1361.

24 Z. Mao,W. Senevirathna,J. Y. Liao,J. Gu,S. V. Kesava,C. Guo,E. D. Gomez,G. Sauvé, *Adv. Mater.,* 2014, **26**, 6290-6294.

25 W. Senevirathna,G. Sauve, *J. Mater. Chem. C,* 2013, **1**, 6684-6694.

26 S. Pejić,A. M. Thomsen,F. S. Etheridge,R. Fernando,C. Wang,G. Sauvé, *J. Mater. Chem. C,* 2018, **6**, 3990-3998.

27 G. Sauve, *Chem. Rec.,* 2019, **19**, 1-16.

28 W. Senevirathna,J.-y. Liao,Z. Mao,J. Gu,M. Porter,C. Wang,R. Fernando,G. Sauvé, *J. Mater. Chem. A,* 2015, **3**, 4203-4214.

29 R. Fernando,S. Pejić,A. Thomsen,C. Wang,G. Sauvé, *Dyes Pigm.,* 2019, **168**, 257-263.

30 F. S. Etheridge,R. J. Fernando,S. Pejić,M. Zeller,G. Sauvé, *Beilstein J. Org. Chem.,* 2016, **12**, 1925-1938.

31 L. Gao,S. Tang,L. Zhu,G. Sauve, *Macromolecules,* 2012, **45**, 7404-7412.

32 M. Ozdemir,D. Choi,Y. Zorlu,B. Cosut,H. Kim,C. Kim,H. Usta, *New J. Chem.,* 2017, **41**, 6232-6240.

33 T. S. Teets,D. V. Partyka,J. B. Updegraff,T. G. Gray, *Inorg. Chem.,* 2008, **47**, 2338-2346.

34 T. S. Teets,D. V. Partyka,A. J. Esswein,J. B. Updegraff,M. Zeller,A. D. Hunter,T. G. Gray, *Inorg. Chem.,* 2007, **46**, 6218-6220.

35 T. S. Teets,J. B. Updegraff,A. J. Esswein,T. G. Gray, *Inorg. Chem.,* 2009, **48**, 8134-8144.

36 L. Gao,N. Deligonul,T. G. Gray, *Inorg. Chem.,* 2012, **51**, 7682-8.

37 C. M. Proctor,M. Kuik,T.-Q. Nguyen, *Prog. Polym. Sci.,* 2013, **38**, 1941-1960.

38 M. M. Mandoc,W. Veurman,L. J. A. Koster,B. de Boer,P. W. M. Blom, *Adv. Funct. Mater.,* 2007, **17**, 2167-2173.

39 K. S. Nalwa,H. K. Kodali,B. Ganapathysubramanian,S. Chaudhary, *Appl. Phys. Lett.,* 2011, **99**, 263301.

40 C. Brabec,A. Cravino,D. Meissner,N. S. Sariciftci,T. Fromherz,L. Sanchez,J. C. Hummelen, *Adv. Funct. Mater.,* 2001, **11**, 374-380.

41 N. A. Unlu,S. O. Hacioglu,G. Hizalan,D. E. Yildiz,L. Toppare,A. Cirpan, *J. Electrochem. Soc.,* 2017, **164**, G71-G76.

42 F. Laquai,D. Andrienko,R. Mauer,P. W. Blom, *Macromol. Rapid Commun.,* 2015, **36**, 1001-25.

43 Y. Liu,C. C. Chen,Z. Hong,J. Gao,Y. M. Yang,H. Zhou,L. Dou,G. Li,Y. Yang, *Sci Rep,* 2013, **3**, 3356.

44 J. Zhou,Y. Zuo,X. Wan,G. Long,Q. Zhang,W. Ni,Y. Liu,Z. Li,G. He,C. Li,B. Kan,M. Li,Y. Chen, *J. Am. Chem. Soc.,* 2013, **135**, 8484-8487.

45 C. Wang,Z. Zhang,S. Pejić,R. Li,M. Fukuto,L. Zhu,G. Sauvé, *Macromolecules,* 2018, **51**, 9368-9381.

46 T. Erb,U. Zhokhavets,G. Gobsch,S. Raleva,B. Stühn,P. Schilinsky,C. Waldauf,C. J. Brabec, *Adv. Funct. Mater.,* 2005, **15**, 1193-1196.

47 M.-Y. Chiu,U. S. Jeng,C.-H. Su,K. S. Liang,K.-H. Wei, *Adv. Mater.,* 2008, **20**, 2573-2578.

48 T. Mueller,R. Gresser,K. Leo,M. Riede, *Sol. Energy Mater. Sol. Cells,* 2012, **99**, 176-181.

49 M. Lorenz-Rothe,K. S. Schellhammer,T. Jaegeler-Hoheisel,R. Meerheim,S. Kraner,M. P. Hein,C. Schuenemann,M. L. Tietze,M. Hummert,F. Ortmann,G. Cuniberti,C. Koerner,K. Leo, *Adv. Electron. Mater.,* 2016, **2**, 1600152.

50 S. Y. Leblebici,L. Catane,D. E. Barclay,T. Olson,T. L. Chen,B. Ma, *ACS Appl. Mater. Interfaces,* 2011, **3**, 4469-4474.

51 Z. Li,J. D. A. Lin,H. Phan,A. Sharenko,C. M. Proctor,P. Zalar,Z. Chen,A. Facchetti,T.-Q. Nguyen, *Adv. Funct. Mater.,* 2014, **24**, 6989-6998.

52 Q.-Q. Pan,Z.-W. Zhao,Y. Wu,Y. Geng,M. Zhang,Z.-M. Su, *J. Taiwan Inst. Chem. Eng.,* 2019, **100**, 160-167.

53 Y. Qin,M. A. Uddin,Y. Chen,B. Jang,K. Zhao,Z. Zheng,R. Yu,T. J. Shin,H. Y. Woo,J. Hou, *Adv. Mater. (Weinheim, Ger.),* 2016, **28**, 9416-9422.

54 M. Zhang,X. Guo,W. Ma,H. Ade,J. Hou, *Adv. Mater.,* 2014, **26**, 5880-5.

This new non-planar non-fullerene acceptor has low synthetic complexity and shows good performance with P3HT, leading to high industrial accessibility.